Conf-9110359--1

Note: This is a preprint of a paper submitted for publication. Contents of this paper should not be quoted or referred to without permission of the author(s).

CONF-9110359--1

DE92 010647

Submitted for publication in *Proceedings of International School on Electron Microscopy in Materials Science*, Brindisi, Italy, October 7–11, 1991

High-Resolution Imaging in the Scanning Transmission Electron Microscope

S. J. Pennycook and D. E. Jesson

SOLID STATE DIVISION
OAK RIDGE NATIONAL LABORATORY
Managed by
MARTIN MARIETTA ENERGY SYSTEMS, INC.
under
Contract No. DE-AC05-84OR21400
with the
U.S. DEPARTMENT OF ENERGY
Oak Ridge, Tennessee 37831-60230

March 1992

HIGH-RESOLUTION IMAGING IN THE SCANNING TRANSMISSION ELECTRON MICROSCOPE

S. J. Pennycook and D. E. Jesson
Solid State Division, Oak Ridge National Laboratory
Oak Ridge, Tennessee 37831-6030, USA

ABSTRACT

The high-resolution imaging of crystalline materials in the scanning transmission electron microscope (STEM) is reviewed with particular emphasis on the conditions under which an incoherent image can be obtained. It is shown that a high-angle annular detector can be used to break the coherence of the imaging process, in the transverse plane through the geometry of the detector, or in three dimensions if multiphonon diffuse scattering is detected. In the latter case, each atom can be treated as a highly localized independent source of high-angle scattering. The most effective fast electron states are therefore tightly bound *s*-type Bloch states. Furthermore, they add constructively for each incident angle in the coherent STEM probe, so that *s* states are responsible for practically the entire image contrast. Dynamical effects are largely removed, and almost perfect incoherent imaging is achieved. *s* states are relatively insensitive to neighboring strings, so that incoherent imaging is maintained for superlattices and interfaces, and supercell calculations are unnecessary. With an optimum probe profile, the incoherent image represents a direct image of the crystal projection, with compositional sensitivity built in through the strong dependence of the scattering cross sections on atomic number *Z*.

1. Introduction

The STEM is a versatile instrument capable of generating many signals for the imaging and analysis of materials at high spatial resolution.[1-3] It is elastic scattering, however, which presents the largest cross section to an incoming electron beam, and will therefore provide the maximum signal-to-noise ratio in a high-resolution image. Elastically scattered electrons have been used to image crystal structures since the earliest days of electron microscopy, from the imaging of crystal defects by diffraction contrast to lattice imaging using phase contrast techniques. However, until recently it had become accepted fact that it was impossible to form an incoherent image at high resolution.[4,5] The main purpose of this review is therefore to outline the physical basis under which this can be achieved. Elastic scattering is defined to include those electrons that have emitted or absorbed one or more phonons, since the energy changes associated with these processes are not observable on present-day instruments.

Elastically scattered electrons carry compositional information through the *Z* dependence of the scattering cross section, which varies approximately as $Z^{3/2}$ if the total elastic scattering is collected, increasing towards Z^2 at higher

scattering angles corresponding to Rutherford scattering off an unscreened nucleus. The high available flux combined with its compositional sensitivity was the motivation for the development of STEM by Crewe and coworkers in the late 1960s and early 1970s.[6,7] With their development of a high brightness field emission gun, it became practically possible to form a finely focussed probe, and impressive images were obtained of individual atoms and small clusters supported on thin carbon films using an annular detector to capture a large fraction of the scattered flux. Furthermore, ratio techniques were developed to suppress the signal from the light support film, the first "Z-contrast" technique in electron microscopy.[8,9]

Despite the fact that such images were formed with coherently scattered electrons, certain incoherent characteristics were clearly apparent. Isolated atoms and small clusters were imaged with improved resolution, comparable to the expected probe intensity profile, and showed no contrast reversals. Section 2 shows that such images can be considered incoherent in the transverse plane, provided the wide angular range of the detector averages a sufficient number of interference fringes and the inner detector angle is much larger than the semiangle of the objective (probe-forming) aperture. The geometry of the detector cannot, however, destroy the coherence of a column of atoms along the beam direction. This can only be destroyed by the physics of the scattering process, by ensuring that the detected signal is dominated by multiphonon scattering events.

The high-angle detector was proposed by Howie in 1979 to improve the visibility of small catalyst particles on light supports, particularly polycrystalline supports.[10] Attempts to apply the ratio techniques of Crewe and coworkers to materials science problems had proved unsuccessful, since with three-dimensional samples, coherent scattering becomes more and more confined to specific Bragg reflections and, therefore, increasingly sensitive to the exact crystal orientation. Any Z-contrast that might be present could easily be swamped by diffraction contrast effects. Howie realized that by increasing the inner angle of the detector from the 20 mrad or so typical of the Crewe annular detector to 40 mrad or higher, the detected signal could be dominated by diffuse scattering, which would be substantially less sensitive to crystal orientation (varying only as a result of channeling effects on the incident probe), and that in addition the image would show enhanced Z-contrast (approaching Z^2). This has proved highly successful and has found numerous applications to catalysis (see Treacy and Rice[11] and references therein), though naturally the efficiency of the imaging process is sacrificed.

In view of the critical role played by a high-angle detector in the realization of incoherent imaging at atomic resolution, it is proposed that the high-angle detector be referred to as the Howie detector. It establishes the

three-dimensional incoherence that allows each atom to be regarded as an independent highly localized source, scattering with a specific high-angle cross section. This is an important contribution to the Bloch state filtering effect described in Section 3, which extends incoherent imaging to thick crystals. This localized, incoherently generated, high-angle scattering, together with the coherent STEM probe, means that *s*-type Bloch states are almost entirely responsible for the image contrast, and dynamical effects, which are due to the interference of Bloch states of comparable amplitude are therefore reduced to second order.[12,13]

That incoherent imaging is obtained even in relatively thick samples is of great utility in the study of materials. Furthermore, since the *s* states of each column are themselves highly localized, individual columns generally contribute to the image independent of their neighbors. Incoherent imaging is maintained for arbitrary arrangements of strings, for example with interfaces, superlattices, and complex unit cells. The integrated *s*-state intensity varies remarkably little for columns of different composition, so that the dominant contribution to the columnar scattering power remains its high angle scattering cross section. A crystalline object can be represented by an object function, a regular array of sharp spikes at each projected column position representing the columnar scattering power, which is then convoluted with the probe intensity profile to give the final image. Section 4 describes how to choose an optimum probe so that the image will directly reflect the local structural and compositional information contained in the object function.

For the first time, therefore, it is possible to achieve a *direct* image of the crystal with atomic resolution. The optimum probe is sample independent, and all columns contribute to the image in a simple and predictable manner, even to below the resolution of the image. It becomes possible to deduce unknown structures directly from the image, to bypass the inversion problem of phase contrast coherent imaging. Instead of basing image interpretation on simulations of likely model structures, the Z-contrast image itself suggests the likely actual structure, which can then be refined through simulation. The importance of this can be judged from the examples presented in Section 5, showing some unanticipated interface structures that have been revealed by direct imaging, together with the insights that this has allowed into the growth and properties of materials.

2. Coherent or Incoherent Imaging?

Whether it is necessary to consider the coherent nature of the scattering process in calculating an image intensity, or whether incoherent imaging theory can be used, depends on the extent to which the final signal is dominated by any particular phase relationship. As more routes of

comparable amplitude but uncorrelated phases contribute to the detected signal, then the intensity approaches more and more closely the incoherent result

It is customary to decompose the elastic scattering from a crystal into a coherent component (Bragg scattering) and a thermal diffuse component (TDS). Averaging over the thermal vibrations of a crystal has the effect of multiplying the shape factor surrounding each reciprocal lattice point by the Debye-Waller factor e^{-2Ms^2}, $M = 8\pi^2\bar{u}^2$, where $\bar{u}^2$ is the mean square atomic vibration amplitude, $s = \theta_B/\lambda$, θ_B is the Bragg angle, and λ the electron wavelength. The lost intensity is redistributed between the Bragg spots, at low angles sometimes in the form of streaks reflecting the spectrum of dominant single phonon excitations, but more uniformly at higher angles as multiphonon processes become more important.

This decomposition is illustrated in Fig. 1 for the case of a single Si atom at room temperature. A detector optimized for collection efficiency, as used by Crewe and coworkers, will obviously detect primarily coherent scattering. By increasing the inner angle, however, this component can be reduced and eventually replaced entirely by the diffuse scattering, although at the expense of a significantly reduced signal.

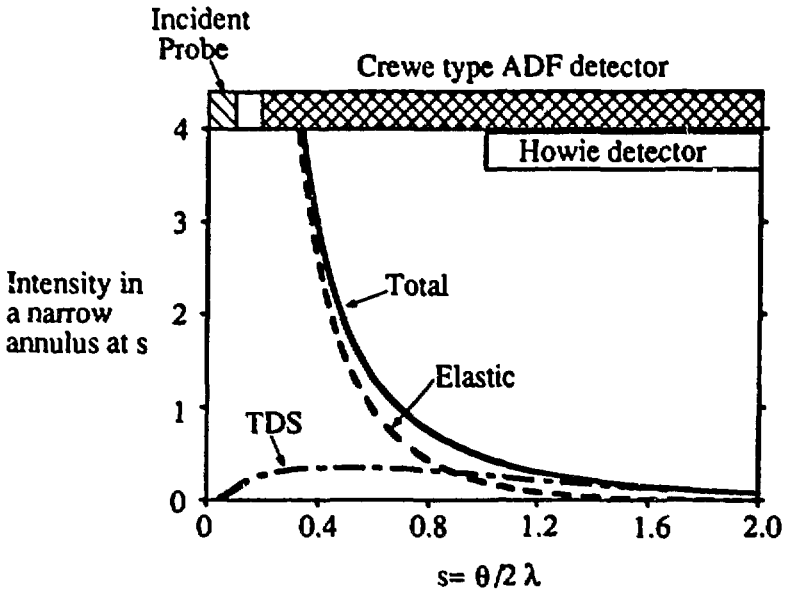

Fig. 1. Plots of the total, elastic, and thermal diffuse scattering (TDS) from a single Si atom at room temperature integrated over a narrow annulus at $s = \theta/2\lambda$, calculated with Doyle-Turner parameters[27] and M = 0.45. Also shown are the typical angular ranges for the objective aperture, the low-angle detector, and the Howie detector.

2.1. *Transverse Incoherence*

We first discuss the distribution of coherent scattering reaching an annular detector and the extent to which interference fringes can be averaged by choosing a suitable detector geometry.[14,15] Consider a *monolayer* crystal with a unit cell 4Å square, containing two atoms per cell, as shown in Fig. 2a. The diffraction pattern for an optimum incident probe located centrally between the two atoms of a cell is shown in Fig. 2b. (The optimum probe at 100 kV accelerating voltage and 1.3 mm objective lens spherical aberation coefficient has 2.2 Å FWHM intensity for 10.3 mrad semiangle and -700 Å defocus). Note that the atomic scattering factor has been suppressed to reveal the vertical fringe system clearly. If atoms were really point scatterers, the detector shown would average the interference fringes very efficiently. However, real atoms are not point scatterers, and the resulting falloff in atomic scattering factor means that the signal detected is dominated by a rather narrow annulus around the inside of the detector. To average over many interference fringes it is clear that the inner detector angle θ_1 must be large compared to the fringe separation, i.e.

$$\theta_1 \gtrsim \lambda/d \ , \tag{1}$$

where d is the separation of the two atoms.

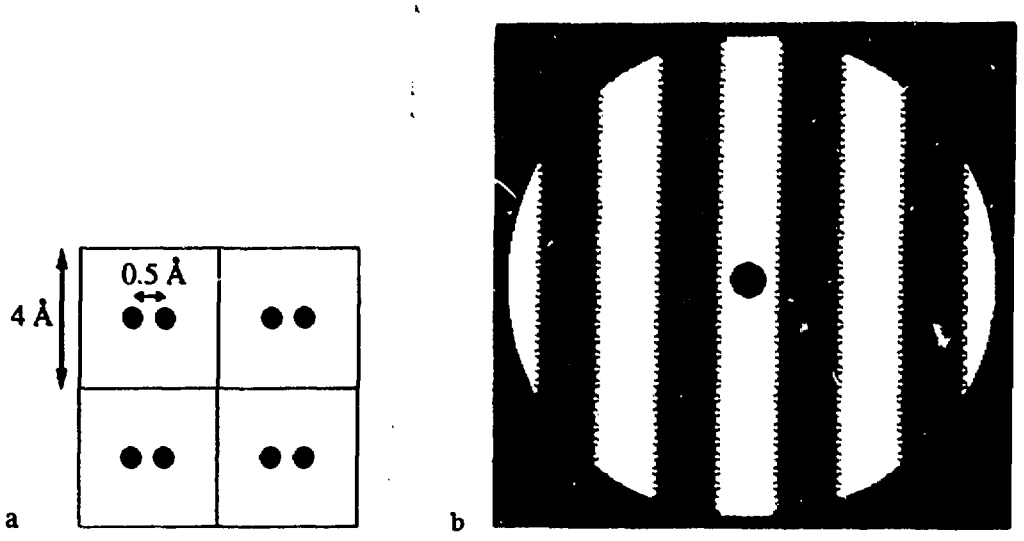

Fig. 2. (a) Square lattice of δ-function potentials. (b) Corresponding diffraction pattern for a probe located midway between two potential spikes.

Figure 3 plots the ratio of the intensity detected from two Si atoms spaced 1.0 and 1.5 Å apart to that expected if the scattering were incoherent, as a function of inner detector angle for an optimum probe placed centrally between the two atoms. At $\theta_1 = 1.22\,\lambda/d$, the detected intensity differs by less than 5% from the incoherent result and we refer to this situation as transverse incoherence.

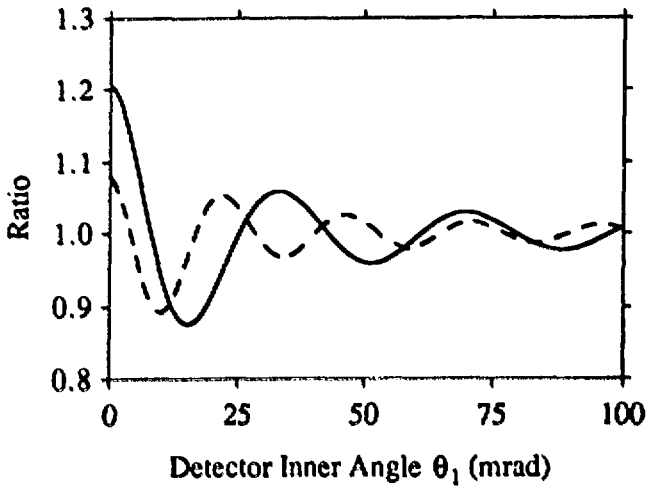

Fig. 3. Ratio of detected intensity to the incoherent result for two Si atoms separated by 1.0 Å (solid line) and 1.5 Å (dashed line) as a function of inner detector angle θ_1.

This should not be taken to imply that for well separated atoms a low angle detector will result in incoherent imaging, since it is also necessary that the inner detector angle be much larger than the angular width of the incident probe

$$\theta_1 >> \alpha \quad , \tag{2}$$

where α is the objective aperture semiangle. Then the probe acts as a simple scaling factor (in real space) for the high-angle scattering potential; atoms act as if they were true point scatterers, and their intensity profile in the image accurately maps the intensity profile of the probe itself.

Previous discussions of the STEM imaging of phase objects have always considered a detector for which $\theta_1 = \alpha$. This leads to the well-known "hole in the detector problem" and the erroneous conclusion that incoherent imaging can only be achieved if *all* the scattered radiation is detected. This in turn leads to the conclusion that incoherent imaging is impossible with a high-resolution probe, since it would necessitate a large hole in the annular detector.[4,5] However, simply by increasing the inner detector angle, the problem is avoided, and incoherent imaging is achieved.

At least with the monolayer crystal discussed so far, we therefore see the usual advantages of incoherent imaging; the image contrast is controlled by the probe *intensity* profile, and shows the expected improvement in resolution and lack of contrast reversals compared to phase contrast imaging which involves interference of the probe *amplitude* profile. This analysis explains the incoherent characteristics apparent from the calculations of Engel.[16] In the next section, we consider the imaging of three-dimensional objects.

2.2. *z-Coherence*

The geometry of the detector is much less efficient at averaging coherence effects between atoms aligned along the beam direction.[17,18] If a second raft of atoms is placed directly behind the first, and viewed from the direction θ, the path difference between atoms in the two layers (see Fig. 4a) is

$$z(1-\cos\theta) \sim z\theta^2/2 \ . \qquad (3)$$

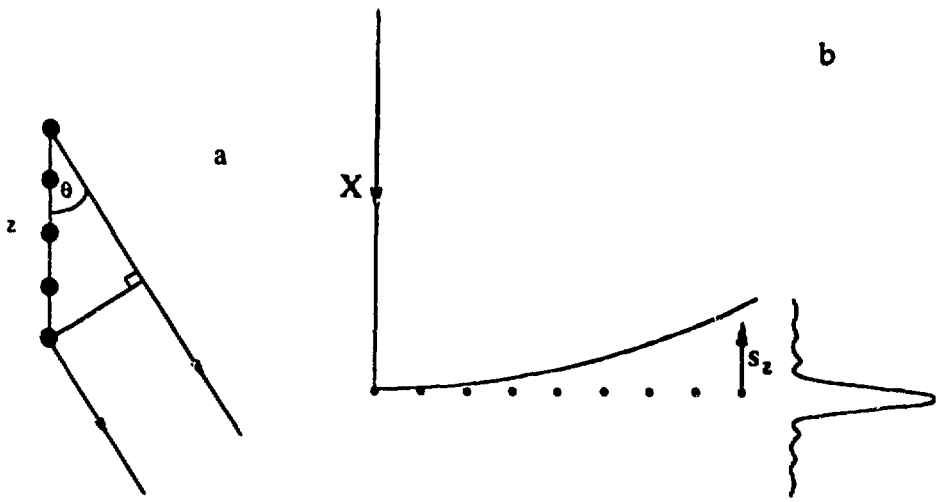

Fig. 4. Scattering geometry for a column of atoms, length z, viewed from a direction θ in (a) real space and (b) reciprocal space showing the Ewald sphere and the shape factors.

Thus for separations

$$z << 2\lambda/\theta^2 \ , \qquad (4)$$

the scattered amplitude from the two rafts will be practically in phase, resulting in a fourfold increase in detected intensity. As further rafts are added to build a three-dimensional crystal, the phase factors from the individual layers must be integrated, giving a total amplitude

$$A(\theta) = \int_0^t e^{-2\pi i s_z z}\, dz \tag{5}$$

where $s_z = \theta^2/2\lambda$ is the deviation parameter, and

$$|A(\theta)|^2 = \left(\frac{\sin \pi s_z t}{\pi s_z}\right)^2 \tag{6}$$

represents the usual kinematic shape factor shown in reciprocal space in Fig. 4b. Note that for axial illumination, if the crystal thickness is much greater than $2\lambda/\theta^2$, then there is substantial destructive interference from atoms at different depths, and very little resultant scattered amplitude from the column as a whole. This is seen by the fact that the Ewald sphere cuts only the tails of the shape factors. There is no way that detector geometry alone can make the Ewald sphere intersect the central maximum of the high angle reflections. Thus if we use a high inner angle to ensure transverse incoherence, the intensity from a crystal will increase initially as t^2, but as destructive interference sets in it will become oscillatory as shown in Fig. 5.

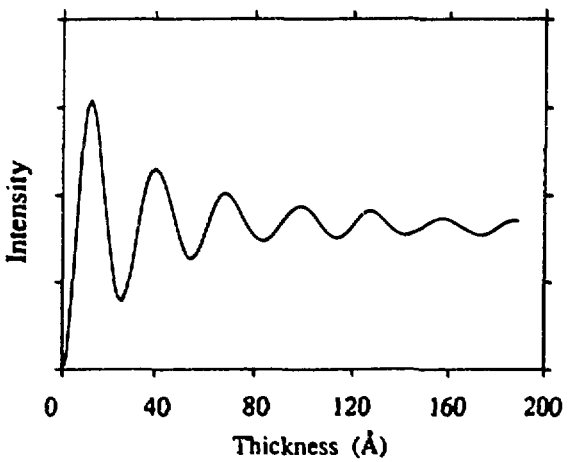

Fig. 5. Thickness dependence of the intensity detected with an optimum probe located centrally over a dumbell in Si(110), detector angles 50–150 mrad.

The behavior can be seen most clearly in the diffraction pattern shown in Fig. 6. This is the same square lattice of point scatterers which was shown in Fig. 2, but now 25 layers are stacked to a total thickness of 100 Å. The radial

fringe system corresponding to the z shape factors is clearly seen, and, since the atomic scattering factor has again been suppressed, this is the only reason that the intensity now falls off with increasing angle (as the Ewald sphere intersects subsidiary maxima of reducing intensity, see Fig. 4b). With increasing crystal thickness, the entire fringe system moves inwards, and the most intense fringe falls inside the hole in the detector, creating the oscillatory behavior seen in Fig. 6. As long as the thickness behavior is appreciated, this does represent a useful imaging mode for phase objects such as small particles (e.g., catalyst clusters) and very thin crystals in general. A larger fraction of the total scattering is collected compared with the method described in Section 2.3, which requires diffuse scattering to dominate the detected signal, larger inner detector angles, and consequent loss of imaging efficiency.

Fig. 6. Diffraction pattern from the projected potential of Fig. 2a, but for a crystal thickness of 100 Å. z-defocussing results in lost intensity, cf. Fig. 2b.

Although we have presented a kinematical discussion, calculations indicate that dynamical diffraction alters this behavior very little, since high angle reflections are generated kinematically even when the low order reflections become dynamical. The only high angle reflections which do not follow this pattern are those in the upper Laue layers which are cut near their peaks by the Ewald sphere. However, it is simple to determine, experimentally or theoretically, whether these HOLZ reflections dominate the integrated intensity reaching the annular detector.[13] Under normal conditions, (room temperature samples, and an annular detector that covers a wide angular range), they are insignificant, being swamped by the zero layer reflections in thin crystals, and by the diffuse scattering in thicker crystals.

2.3. *Diffuse Scattering*

Although detector geometry alone cannot destroy the coherence along a column of atoms, in conjunction with the crystal's thermal vibrations, this coherence can effectively be broken. A periodic modulation in the lattice spacing with wavevector q generates sidebands at ± q around each reciprocal lattice point, having the same shape factor as the main Bragg reflection. At low angles this can result in streaks corresponding to the excitation of dominant single phonon modes in a particular direction, although if more than one phonon is involved in the scattering event, a diffuse background will always result. This is the situation for high scattering angles where multiphonon scattering is an order of magnitude more probable than single-phonon scattering, as shown clearly by Hall.[19] The sidebands form a broad, continuous distribution in reciprocal space, with the result that as a large number of individual multiphonon scattering events contribute to an image, the Ewald sphere samples all points on the shape factor. Since

$$\int_{-\infty}^{\infty} \left(\frac{\sin \pi s_z t}{\pi s_z}\right)^2 ds_z = t \ , \tag{7}$$

the intensity detected from the column of atoms is now precisely the intensity that would have been detected if the atoms were acting as incoherent emitters of electrons. Note that this is an *effective* incoherence along the column, since there is insufficient z-momentum transfer to localize the scattering event at a single atom in the column.

The Einstein model of independently vibrating atoms is therefore the ideal model for this situation, and we can construct a 2D projected potential $V^{HA}(\mathbf{R})$ to describe the diffuse scattering generated incoherently by the unit cell at position R. The total intensity reaching the detector I^{HA} will then be given by the total rate of loss from the incident wavefield $\psi(\mathbf{r})$,

$$I^{HA} = \frac{2}{\hbar v} \int |\psi(\mathbf{r})|^2 V^{HA}(\mathbf{R})\, d\mathbf{r} \ , \tag{8}$$

which is exactly analogous to the calculation of absorption effects in dynamical diffraction,[20] and the generation of X rays[21] or low-energy photons.[22] In fact, explicit expressions for $V^{HA}(\mathbf{R})$ can be obtained following the treatment of Hall and Hirsch.[20] Their approach involves integrating the total time averaged scattering over the appropriate angular range, in our case the annular detector, and subtracting out the Bragg scattering. All multiphonon contributions are automatically included, and the Fourier components of $V^{HA}(\mathbf{R})$ are given by

$$V_g^{HA} = \frac{-\hbar^2}{2m_o}\frac{4\pi}{\Omega}\sum_\kappa e^{-ig\cdot r_\kappa} f_\kappa^{HA}(s,M)e^{-M_\kappa s^2} \qquad (9)$$

where

$$f_\kappa^{HA}(s,M) = \frac{2h\gamma^2}{m_o v}\int_{\text{detector}} f_\kappa(|s'|) f_\kappa(|s-s'|)\left[1-e^{-2M_\kappa(s'^2-s\cdot s')}\right]d^2s' \qquad (10)$$

Here f is the atomic scattering factor, Ω is the volume of the unit cell, v is the electron velocity, and

$$g = 4\pi s = 2\pi\theta/\lambda\,. \qquad (11)$$

It should be emphasized that the single phonon model of Wang and Cowley[23,24] is entirely inappropriate for describing high-angle scattering, since it is based on the small-angle approximation of Takagi.[25] It ignores entirely the multiphonon contribution which dominates at high angles and therefore predicts a much reduced diffuse component, as well as an unphysical doughnut-shaped scattering potential which is not peaked at the projected atom sites. More recent attempts to include such processes into the multislice formulation have incorrectly summed the multiphonon contributions, and therefore preserve the unphysical form of the scattering potential.[26]

If we now consider the case of a Howie detector, some useful simplifications can be made which provide significant insight into the nature of the imaging. Since the inner detector angle is much larger than the scattering angles of the strongly excited low order beams, only low order Fourier components V_g^{HA} contribute in Eq. (8). Therefore, since s' is confined to the detector, we have s' >> s in the integrand of Eq. 10, which then reduces to

$$f_\kappa^{HA}(s,M) \approx \frac{2h\gamma^2}{m_o v}\int_{\text{detector}} f_\kappa^2(|s'|)\left[1-e^{-2M_\kappa s'^2}\right]d^2s'\,. \qquad (12)$$

The integral over the detector becomes independent of s, and takes the form of a simple cross section. In real space this condition implies that the high angle scattering potential is sharply peaked on the scale of the incident probe wavefunction, so that Eq. (8) can be approximated by

$$I^{HA} = \frac{2}{\hbar v}\sum_\kappa |\psi(r_\kappa)|^2 \int V^{HA}(R)dR = \sum_\kappa |\psi(r_\kappa)|^2\,\sigma_\kappa \qquad (13)$$

where

$$\sigma_K = \left(\frac{4\pi\gamma}{\chi}\right)^2 \int_{\text{detector}} f_K^2(s)\left[1 - e^{-2M_K s^2}\right] d^2s \qquad (14)$$

Thus, in this approximation of complete localization, the high angle form of the scattering factor is identical to that for isolated atoms, which was shown in Fig. 1, and the total intensity scattered by each atom is proportional to the incident electron intensity at its site. The detector has been effectively transferred to the atom sites themselves.

The appropriate scattering factors must of course correctly describe the high-angle scattering from isolated atoms. The usual Doyle and Turner[27] scattering factors are calculated in the first Born approximation, and, although appropriate for dynamical diffraction calculations, lead to substantial errors in calculating the diffuse scattering at high angles, especially for heavier elements. Figure 7 compares some experimental measurements with theoretical predictions for the ratio of Bi to Si cross sections.[28] To highlight the failure of the Born approximation, the ratio is expressed in terms of

$$\eta = \frac{\sigma_{Bi}}{\sigma_{Si}} \cdot \frac{Z_{Si}^2}{Z_{Bi}^2}, \qquad (15)$$

which removes the strong Z dependence of the cross sections ($\eta = 1$ for unscreened Rutherford scattering). The Born approximation cross sections predict a relative scattering power of Bi to Si almost twice as great as that observed experimentally, (though for species which differ less in their relative atomic number the error is correspondingly reduced).

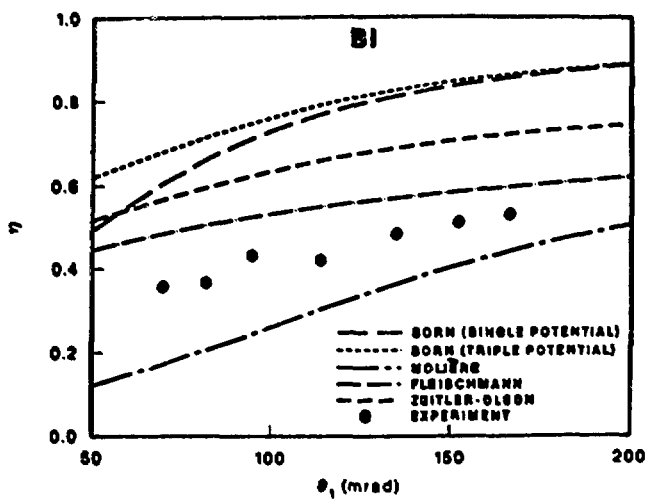

Fig. 7. Comparison of various analytical expressions with experimental measurements of the full high-angle atomic cross sections.

A useful analytical approximation was proposed by Fleischmann,[29] which can be directly integrated over the annular detector to give

$$\sigma \propto Z^2 \left[\frac{\theta_2 - \theta_3}{\theta_1 \theta_2 \theta'_\alpha} + \frac{1}{\theta'^2_\alpha} \ln \frac{\theta_1}{\theta_2} \cdot \frac{(\theta_2 + \theta'_\alpha)}{(\theta_1 + \theta'_\alpha)} \right] \tag{16}$$

where θ_1 and θ_2 are the inner and outer detector angles and θ'_α is a modified screening angle given as

$$\theta'^2_\alpha = e\, \theta_0^2 \,(1.13 + 3.76\, \alpha^2) \tag{17}$$

where $\alpha = Z/137\,\beta$, $\beta = v/c$, v is electron velocity, and $\theta_0 = 1.13\, Z^{1/3}/137\,\beta$, the Born screening angle.

Note that this convenient integrated cross section does not include the Debye Waller factor [the term in square brackets in Eq. (14)], which can significantly alter the effective strength of different strings. More accurate partial wave calculations of atomic scattering factors have also been performed,[30] (see the contribution by Salvat).

3. Incoherent Imaging at Atomic Resolution

Consider a Howie detector with sufficient inner angle to establish effective three-dimensional incoherence, so that the intensity reaching the detector is given by Eq. (8). To form a high resolution image, the wave-function in the crystal must clearly be localized on a scale comparable with the separations of the atomic columns, which requires a high-resolution, probe-forming objective lens. Equation (8) can then be used to predict how the detected intensity will vary as the probe is scanned over a sample.

For high source demagnification, the objective aperture can be considered coherently illuminated by an axial plane wave, and the probe is just the phase aberrated spherical wave produced by transfer through the objective lens,

$$P(R\text{-}R_0) = \int_{\substack{\text{objective} \\ \text{aperture}}} e^{i[K \cdot (R - R_0) + \gamma(K)]} dK \tag{18}$$

where K is the transverse component of the incident wave vector and

$$\gamma = \frac{\pi}{\lambda}\left(\Delta f\theta^2 + \frac{1}{2}C_s\theta^4\right) \tag{19}$$

is the transfer function phase factor for a defocus Δf and spherical aberration coefficient C_s. The probe intensity profile is then $P^2(R\text{-}R_0)$.

3.1. *Incoherent Imaging of a Phase Object*

By definition, a phase object has the convenient property that the probe intensity profile inside the crystal is identical to that of the incident probe. If we project the high angle potential through the entire object, we can write Eq. (8) in the form

$$I^{HA}(R\text{-}R_0) = \frac{2}{\hbar v}\int P^2(R\text{-}R_0)\, V^{HA}(R)\, dR, \tag{20}$$

which is simply a convolution between the incident probe intensity profile $P^2(R)$ and an object function $O(R)$, written in standard incoherent imaging theory as

$$I^{HA}(R) = O(R) * P^2(R). \tag{21}$$

where

$$O(R) = \frac{2}{\hbar v} V^{HA}(R)\ , \tag{22}$$

is the crystal object function. In the limit of complete localization this can be written as

$$O(R) = \sum_{\kappa} \sigma_{\kappa}\, \delta(R - R_{\kappa}) \tag{23}$$

Such an object function is shown schematically in Fig. 8. A raft of Si atoms as seen by the Howie detector appears as an array of sharp spikes, each of the order of 0.1Å in width. These spikes are then weighted by the profile of the probe, so that as the probe scans an array of columns it will effectively map out their scattering cross sections in the form of an incoherent image, a direct image of the crystal projection.

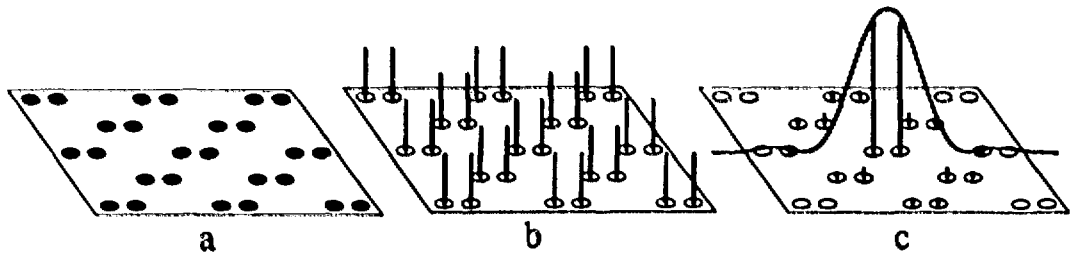

Fig. 8. Schematic showing incoherent imaging of a phase object with a Howie detector: (a) monolayer raft of Si(110), (b) high-angle scattering power, and (c) weighting of spikes with a 2.2 Å probe located over the central dumbbell. As the probe scans, it maps out the spikes, producing a direct image of the high-angle scattering power.

3.2. *Dynamical Effects*

In thicker crystals dynamical diffraction rapidly sets in, both for the incoming probe and the outgoing scattered electrons, though the coherence between these two processes is still effectively destroyed by the multiphonon high-angle scattering events. We may still consider each atom as an independent source of scattering and can, therefore, consider separately the dynamical diffraction of the incoming probe (channeling) and the outgoing electrons (blocking). Such an approach was used, for example, by Bird and Wright[31] to predict Kikuchi line profiles which represent channeling effects on the outgoing electrons and redistribute the intensity on the scale of a few Bragg angles. This would be important for a point detector, but for a Howie detector which covers a large angular range, there is practically no effect on the total intensity falling on the detector, especially if the crystal is in a zone axis orientation so that the strongest Kikuchi lines will be radial and redistribute flux tangentially to the detector. We can, therefore, ignore dynamical effects on the outgoing electrons and the high-angle potential for each unit cell, $V^{HA}(\mathbf{R})$, is the same as before.

The effect of dynamical diffraction is to alter the incident electron intensity at each individual atom site. Equation (8) can still be used to calculate the detected intensity provided these effects are properly included. In general, an electron incident close to a major zone axis has a strong tendency to channel close to the atom sites, resulting in a strong enhancement of localized excitations such as X ray emission and Rutherford scattering. This compensates significantly for the low intrinsic efficiency of a high-angle detector.

Although one might expect that dynamical effects would affect the form of the image in some way, experimentally, the image intensity simply increases with increasing thickness as shown in Fig. 9. Despite the strong interference fringes seen in the bright field image, no fringes are seen in the

high-angle signal, and the form of the high resolution image remains approximately constant to beyond 600 Å in thickness. Eventually, the contrast slowly fades away although no loss in resolution is apparent.

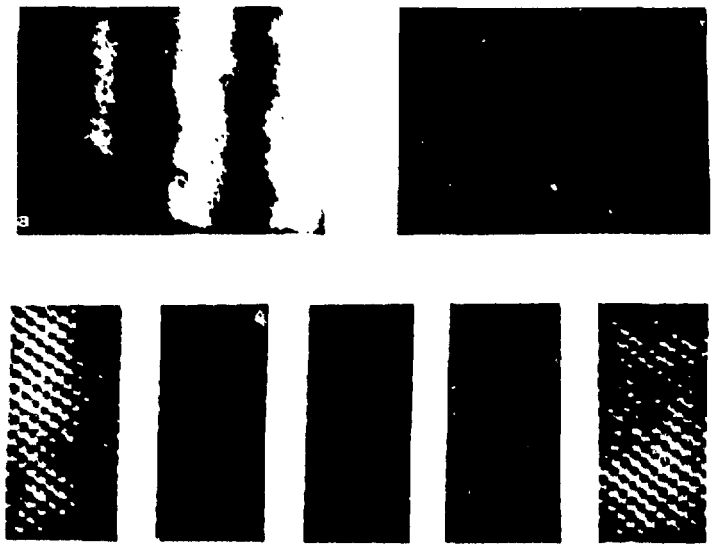

Fig. 9. Si(110) imaged with a 10 mrad objective aperture to exclude the (111) beams. (a) thickness fringe image (bright field). (b) Howie detector image (75–150 mrad), with high magnification images at 120, 230, 350, 470, and 610 Å thickness, (c)–(g).

To see the physical basis for this remarkable behavior we must examine the nature of the Bloch states excited within the crystal. Bloch states are the stationary states of the electron in the crystal, the natural basis states with which to examine the problem. The power of the Bloch wave approach is that dynamical interaction of very many diffracted beams is described very well by the interference of just a few Bloch states. In this case we shall find that the problem simplifies to the extent that only a single Bloch state is important, which is the fundamental reason for the lack of any observable interference effects.

For a plane wave incident on a crystal with wavevector χ (transverse component K), the wave function in the crystal $\psi(r)$ is given by a sum of j Bloch states.

$$\psi(R,z) = \sum_j \varepsilon^j(K)\tau^j(K,R)e^{-is^j(K)z/2\chi}e^{-\mu^j(K)z} \qquad (24)$$

where $\tau^j(K,R) = b^j(K,R)e^{iK\cdot R}$ are the two-dimensional Bloch states of transverse energy $s^j(K)$, absorption $\mu^j(K)$ and excitation coefficients $\epsilon^j(K)$. If the incident electron is in the form of a spherical wave converging to a point R_o, the wave function inside the crystal becomes

$$\psi(R-R_o,z) = \sum_j \int_{\text{objective aperture}} \epsilon^j(K)b^j(K,R)e^{-is^j(K)z/2\chi}e^{-\mu^j(K)z}e^{iK\cdot(R-R_o)}e^{i\gamma(K)}dK \quad (25)$$

a coherent superposition of a whole set of Bloch states corresponding to each incident angle. States which are relatively insensitive to incident angle will therefore add in phase during this angular integration, whereas states which vary significantly with incident angle will destructively interfere.

Figure 10 shows the first six Bloch states for a plane wave electron incident axially on Si<110>. They are similar to a set of molecular orbitals[32,33] comprising bonding and antibonding (denoted by *) combinations of *s* and *p* states, the *s* states peaking near the atomic strings, the *p* states having nodes near the strings. The corresponding dispersion surface is shown in Fig. 11 where it is seen that the s-type molecular orbital states are non-dispersive, due to the fact that states on one dumbbell overlap negligibly with states on neighboring dumbbells. These states therefore dominate the angular integration, and as the probe propagates into the crystal, it tends to take on the form of the *s*-states, forming strong peaks along the atomic columns with a width of the order of 1 Å while showing the envelope of the incident probe profile.[34,35] In contrast, the destructive interference of the p-type states results in a significantly reduced intensity between the columns.

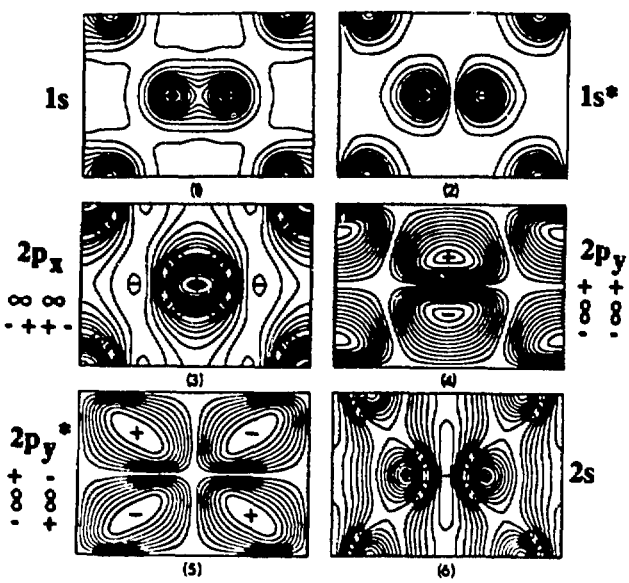

Fig. 10. The first six bloch states for Si(110) at 100 kV with their corresponding molecular orbital interpretations. Polarity is indicated by + or - signs.

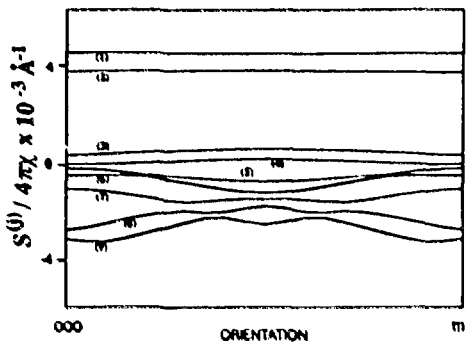

Fig. 11. Section of the dispersion surface for Si(110) at 100 kV.

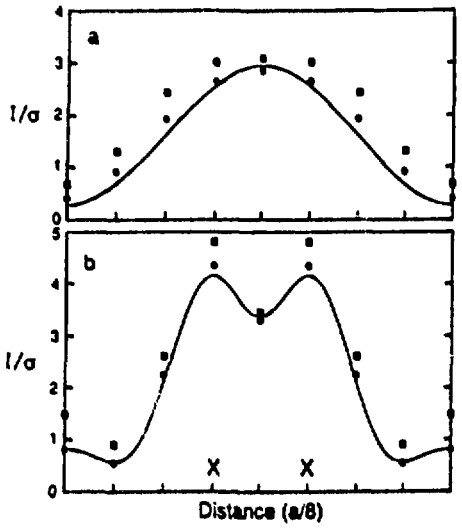

Fig. 12. Image intensity scanning an optimum probe from channel to channel along the [001] direction in Si[110] (atom sites marked X), calculated for accelerating voltages of (a) 100 kV and (b) 300 kV using all Bloch states (squares), s-states only [Eq. (26), circles], and the effective probe approximation [Eq. (27), solid line].

The form of the high angle potential further enhances the effectiveness of this Bloch state filtering effect by coinciding with the peak s state intensity. States of other than s-type symmetry (for example *p*-states) tend to have nodes at the atom sites and, therefore, have a minimum contribution to the electron intensity in this region. Full dynamical calculations for Si(100) have shown that the s-states are responsible for practically the entire image contrast as shown in Fig. 12. Since beating between Bloch states is the origin of dynamical diffraction effects, it is obvious that if only one state dominates, there can be no strong interference effects.

Furthermore, in a perfect crystal the image can again be written in the form of a convolution. If we assume that only *s* states are important, inserting Eq. (25) into Eq. (8) gives

$$I^{HA}(R_o,t) \approx \frac{2}{\hbar v}\int_0^t \Big| \int_{\substack{\text{objective}\\ \text{aperture}}} \varepsilon^{ls}(K)\, b^{ls}(R,K) e^{-is^{ls}(K)z/2\chi} e^{-\mu^{ls}(K)z} e^{iK\cdot(R-R_o)} e^{i\gamma(K)} dK \Big|^2 dz\, V^{HA}(R)\, dR \qquad (26)$$

Since the s states are non-dispersive they may be removed from the angular integration, giving

$$I^{HA}(R_o,t) \approx \frac{2}{\hbar v} \int_0^t \left| \varepsilon^{1s(0)} b^{1s}(R,0) e^{-i s^{1s}(0) z/2\chi} e^{-\mu^{1s}(0) z} \right|^2 dz$$

$$\int \left| \frac{1}{\varepsilon^{1s}(0)} \int_{\substack{\text{objective} \\ \text{aperture}}} \varepsilon^{1s}(K) e^{i[K \cdot (R - R_o) + \gamma(K)]} dK \right|^2 V^{HA}(R)\, dR \qquad (27)$$

which again can be written as the convolution

$$I^{HA}(R,t) = O(R,t) * P^2_{eff}(R) \qquad (28)$$

where O(R,t) is the object function given by

$$O(R,t) = \frac{2}{\hbar v} \varepsilon^{1s^2}(0) b^{1s^2}(R,0) \left(\frac{1 - e^{-2\mu^{1s}(0) t}}{2\mu^{1s}(0)} \right) V^{HA}(R) \qquad (29)$$

and

$$P^2_{eff}(R) = \left| \frac{1}{\varepsilon^{1s}(0)} \int_{\substack{\text{objective} \\ \text{aperture}}} \varepsilon^{1s}(K) e^{i[K \cdot (R - R_o) + \gamma(K)]} dK \right|^2 \qquad (30)$$

is an effective probe intensity profile which includes the angular fall-off in s state excitation. This approximation is shown as the solid line in Fig. 12, and matches the full dynamical result quite closely.

The s states are highly localized about the atomic columns, so that their excitation drops relatively slowly over the range of the objective aperture. The effective probe has therefore practically the same width as the incident probe, and the image resolution is preserved. To a good approximation we can write

$$P^2_{eff} = S^2(K_c) P^2 \ , \qquad (31)$$

where $S(K_c)$ is a scaling factor given by

$$S(K_c) = \int_{\substack{\text{objective} \\ \text{aperture}}} \varepsilon^{1s}(K)dK/\pi K_c^2\, \varepsilon^{1s}(0)\,, \tag{32}$$

which can then be incorporated into the columnar object function [Eq. (29)] to allow the assembly of object functions for more complex arrangements of strings such as large unit cell materials, interfaces and superlattices.

In Eq. (29), $V^{HA}(R)$ is the high angle potential per unit thickness, and the object function is therefore similar to that for the phase object [Eq. (22)], but is now multiplied by the integrated s state intensity along the column, which can be regarded as the channeling effect of that column. In the limit of complete localization, Eq. (29) becomes

$$O(R_i,t) = \sum_i \sigma_i\, \varepsilon^{1s^2}(0) b^{1s^2}(R_i,0) \left(\frac{1-e^{-2\mu^{1s}(0)t}}{2\mu^{1s}(0)} \right) \tag{33}$$

where $\sigma_i = \frac{1}{t}\sum_\kappa \sigma_\kappa$ is the columnar cross section per unit thickness.

Due to the thickness integration, the object function increases monotonically with thickness as shown in Fig. 13 for Si and Ge in the <110> projection. Dynamical effects are strongest at thicknesses of 50-100Å, where the s states are becoming established. A more accurate description of the object function has also been given,[36,37] which includes the interference of the s state with the incident probe and gives a better fit to the full dynamical curve in Fig. 12. Overall however, dynamical effects have been reduced to second order, which highlights the importance of breaking the coherence of the imaging process. The Howie detector is sensitive to the integrated electron intensity at the atom sites, and can appear free from interference effects, while simultaneously the bright field detector is showing very strong thickness oscillations (Fig. 8).

As the crystal thickness increases, the effects of absorption become significant, particularly in the case of Ge where the object function becomes almost flat. However, due to the nature of the convolution we predict no change in resolution; the relative excitation of *s*-states on different atomic columns is controlled by P_{eff}^2, which depends on the probe profile at the crystal entrance surface. As the *s*-states become depleted through absorption, the uniform background intensity from all other states (and from the absorbed electrons themselves) will slowly increase, and we expect a gradual loss in image contrast as observed experimentally.

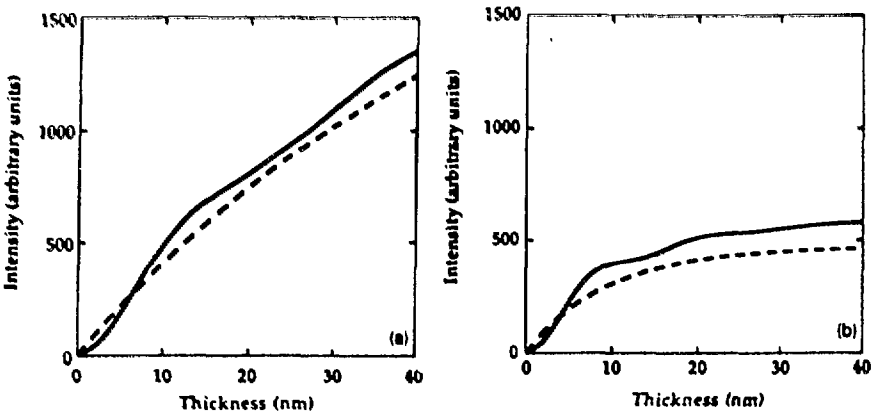

Fig. 13. Thickness dependence of the object function in (a) Si⟨110⟩ and (b) Ge⟨110⟩ calculated using the full dynamical calculation (solid lines) and using the s states alone (dotted lines).

We might also anticipate that since the tightly bound s-states are correspondingly broad in reciprocal space, they would be relatively insensitive to the exact orientation of the crystal. This has been our experimental experience, and recent calculations have confirmed that the electron current follows the strings for tilts of up to half a Bragg angle.[35,38]

4. Image Localization

For a crystal in a zone axis orientation, the object function is highly localized about the projected column locations, and has a strength primarily dependent on the column composition. In thicker crystals the strength also includes the thickness integrated s state intensity as a measure of the channeling effect of the column, but is otherwise free from the effects of dynamical diffraction.

Since the s states are themselves quite localized, they only overlap significantly at rather small column separations. Furthermore, the object function requires only the *intensity* of the s-states, not their eigenvalues. The s state intensity is insensitive to small overlaps with the tails of the potentials from neighboring strings. If the potential from one column is relatively constant over the s-state at a neighboring site, the effect will be similar to a change in the mean inner potential and will only affect the s-state eigenvalue (i.e., the phase with which the state emerges at the exit face of the crystal). Note that in phase contrast imaging, such small changes in the eigenvalue are directly converted to changes in the image intensity,[39] so that strong proximity effects would be likely even if only s-states were involved in the

imaging. Of course, less localized states are also involved in phase contrast imaging, and these are far more sensitive to overlaps with neighboring strings, with the result that proximity effects are inherent and images from interfaces must be calculated explicitly using a complete structure model for the interface. This is the key reason why it is difficult to interpret a phase contrast image directly in terms of likely column positions and scattering powers.

If the spacing between strings does become comparable to the width of the s states, then substantial overlap may occur. This happens in the case of the Si or Ge dumbbells seen in ⟨110⟩ projection (Fig. 10); the s states on the two closely spaced strings comprising the dumbbell overlap to form bonding and antibonding molecular orbital combinations. The intensity at the atom sites is altered by approximately 10% from the intensity at the sites in an isolated column, but can be simply calculated using an appropriate molecular orbital.

In general, s states are the least sensitive states to their surroundings, with the result that the object function at an interface usually shows no proximity effects. Object functions can be assembled column by column using only axial Bloch state calculations and the dispersion surface for model unit cells provided that the string of interest is held at a sufficient separation so that the s state intensity is equal to that of an isolated string.[37] If significant overlap is anticipated, then the appropriate molecular orbital calculations can also be performed with model unit cells. This approach represents a vast saving in computer time compared to full calculations and eliminates the need for supercell calculations.

To convert the highly local object function into a highly local image clearly requires a finely focused probe, but it is important to realize that the highest resolution probe will not necessarily provide a highly local image. This is because the probe is formed from coherent illumination [see Eq. (18)], and can become nonlocal in two ways as seen in Fig. 14. With a small objective aperture and small defocus value, a broad diffraction limited probe results in loss of both resolution and contrast. At large objective apertures and large defocus values, large subsidiary maxima can surround the central peak, and if they coincide with neighboring columns, severe compositional smearing will result. It becomes very difficult to visualize the effect of the convolution with such complicated probe shapes. Note however that such probes do result in a higher image *resolution*, due to the narrowing of the central peak.[40,41] Contrast transfer functions analyze only the spatial frequency content of the probe and do not address the issue of localization.

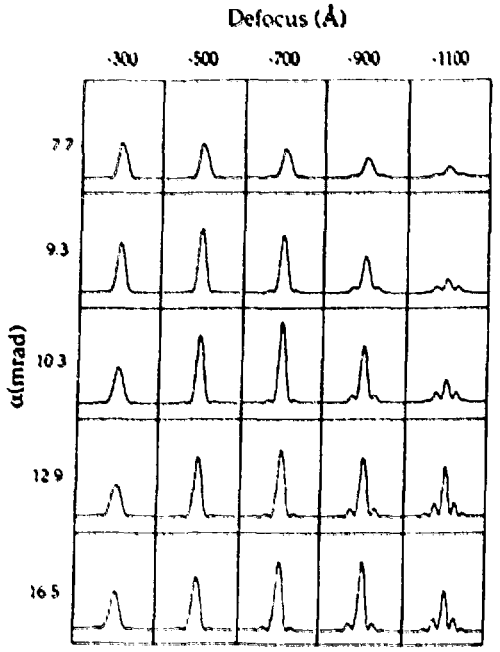

Fig. 14. Effective probe intensity profiles for various objective aperture semiangles α and defocus values calculated for Si⟨110⟩ at 100 kV for C_S = 1.3 mm. The full width of each profile is 20 Å.

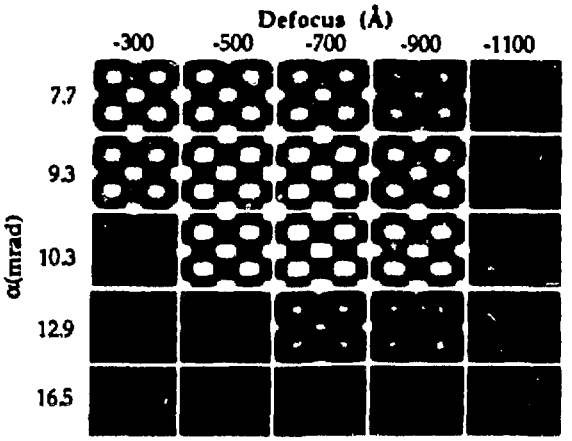

Fig. 15. Simulated images of Si⟨110⟩ corresponding to the probes shown in Fig. 14.

Simulated images corresponding to these probe profiles are shown in Fig. 15. The optimum conditions were analyzed by Scherzer[42] and Crewe and Salzman,[43] who arrived at the conditions

$$\alpha_{opt} = \left(\frac{4\lambda}{C_s}\right)^{1/4} \tag{34}$$

$$\Delta f_{opt} = -(C_s\lambda)^{1/2} \tag{35}$$

which results in a probe intensity profile very similar to an Airy disc in light optics, so that the resolution limit can be defined using a simple two point Rayleigh criterion, as

$$d_{min} = \frac{0.61\,\lambda}{\alpha_{opt}} = 0.43\,C_s^{1/4}\lambda^{3/4} \tag{36}$$

This is very close to the radius of the first intensity minimum and to the FWHM of the central peak. These conditions should not be confused with

the well known Scherzer conditions for phase contrast imaging[42] ($d_{min} = \frac{\lambda}{\alpha} = 0.66\ C_s^{1/4}\lambda^{3/4}$, see also Cowley[44]). Note the significant improvement in resolution expected from incoherent imaging, which allows a crystal to be resolved at much lower voltages than with coherent imaging.

However, defining the resolution in this way tends to obscure the important advantage of incoherent imaging, that is, that the resolution limit is just a definition of when two point sources are distinguishable, (specifically the separation at which the intensity between the two objects dips to around 75% of the peak intensity[45]). For smaller separations, the *shapes* of the image features can be analyzed to recover information at higher spatial frequencies through a suitable deconvolution procedure. One method which is particularly appropriate in the case of a sharp object function is maximum entropy reconstruction,[46] which will be illustrated later.

5. The Importance of Direct Imaging in Materials Science

With an optimum imaging probe, the image represents a map of the materials scattering power, revealing the locations and relative compositions of the atomic columns, truly a direct image of the material with atomic resolution. The optimum probe is sample independent, and all columns contribute to the image in a simple and predictable manner, even to below the resolution of the image, so that it becomes practically possible for the first time to deduce unknown structures directly from the image.

Direct imaging of interface structure and composition can be achieved without the need for any preconceived ideas concerning likely model structures. Unanticipated effects will be immediately apparent and can give dramatic insight into interfacial properties and the growth mechanisms by which such structures arose. Insights into the growth and properties of semiconductors and superconductors have recently been reviewed,[47] and two examples are outlined below.

Semiconductor materials grown by molecular beam epitaxy frequently show interface structures that differ substantially from the model interface structures considered previously, reflecting the crucial role of kinetic factors in low temperature growth. Figure 16 shows part of a Si_4Ge_8 ultrathin superlattice revealing an unexpected complexity in interfacial structure, in fact a different atomic arrangement at each interface.[48] Obviously, such an image is extremely important in attempting to understand the optical properties of the material, but it also directly reflects the atomistic processes which occurred during growth. A very plausible Ge atom pump model involving interchange of a Ge adatom with an underlying Si atom at one of the two district step configurations which occur when a new monolayer

advances over a 2×1 reconstructed surface explains the various ordered arrangements observed and the asymmetric interfacial abruptness. The lateral size of ordered domains correlates well with the size of islands observed by scanning tunneling microscopy.

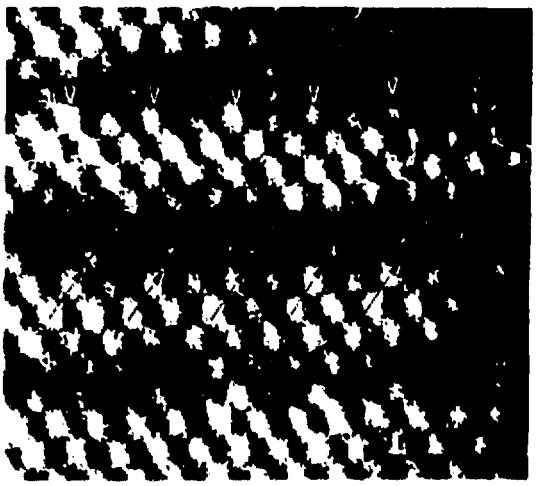

Fig. 16. Complex interfacial arrangements revealed in a Si_4Ge_8 ultrathin superlattice resulting from atom exchange processes during growth.

It is most unlikely that such a complex arrangement of different phases would ever be considered as a likely trial structure for fitting to diffraction data (and even less likely that a fit would be believed). It is also impossible for the atom pump to be seen spontaneously in any molecular dynamics calculation of surface processes due to the extremely short time scales that can be explored. The direct image of the interface structure provides a new depth of insight into materials behavior.

In the case of the superconducting superlattices, the images of Fig. 17 indicate perfect crystallinity but a stepped compositional modulation, which again directly reflects the nature of the growth process.[49] Each interface of the superlattice presents a snapshot of the state of the growing surface at that particular time, a snapshot obtained under the true conditions of supersaturation and left recorded in the microstructure of the film. The surface supersaturation during growth was low enough to allow sufficient surface mobility to avoid structural defects, but high enough that island growth occurred with associated roughening of the growing surface. It is clear that cell-by-cell growth took place, a layer one unit cell thick completing almost perfectly before the next layer nucleated, and the spacing of the steps reflects the intrinsic island size. The origin of this cell-by-cell growth was revealed by imaging an amorphous crystal interface produced by ion implantation (Fig. 18). A striking preference was seen for the crystal to

terminate at the Cu-chain plane, which explains why c-axis perpendicular growth, in units of a complete 11.7 Å high unit cell, is the energetically preferred growth mode. At higher supersaturations this morphology cannot be maintained, and growth proceeds with the a-b plane as the growing surface. Under these conditions, a remarkable roughness was seen on the microscopic scale in the form of pillars one or two unit cells in area extending out of the surface. Such microstructures correlate directly with measured transport properties.[47,49]

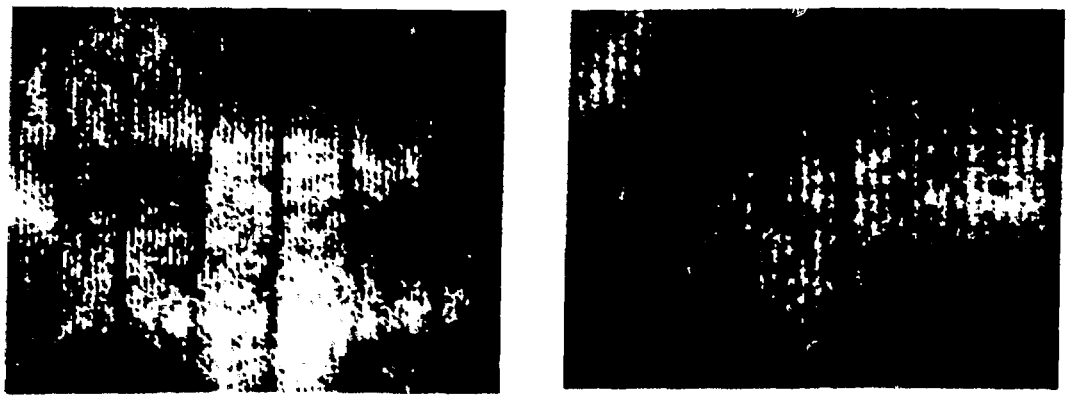

Fig. 17. A superlattice comprising single unit cells of $YBa_2Cu_3O_{7-x}$ separated by nominally 8 unit cells of $PrBa_2Cu_3O_{7-x}$, the growth direction being from left to right. The unit cell steps are a memory of the cell-by-cell growth mode involving the successive nucleation and coalescence of islands.

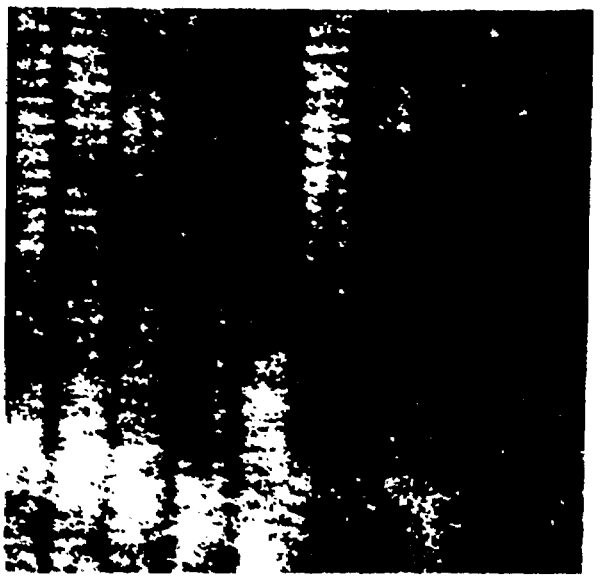

Fig. 18. Cell-by-cell amorphization of $YBa_2Cu_3O_{7-x}$ by oxygen ion implantation revealing the preferred crystal termination to be the Cu-chain plane.

Direct imaging of the actual structures present at interfaces provides deep insight into the origin of materials properties, and into the mechanisms by which such structures arose. Such images provide the long awaited link at the fundamental atomistic level between growth mechanisms, final microstructure, and materials properties.

6. Future Directions

All images so far obtained have used an accelerating voltage of 100 kV in a VG Microscopes HB501UX equipped with a high resolution pole piece with C_S = 1.3 mm, giving a resolution limit of 2.2Å under Scherzer optimum conditions. At 300 kV, the resolution limit reduces to 1.4 Å, which would clarify significantly the available view of a material's structure and chemistry, as indicated by the simulated images of a superlattice in Fig. 19. The smaller probe provides compositional sensitivity for the individual columns comprising the dumbbells. At the time of writing, such a machine is undergoing initial tests.

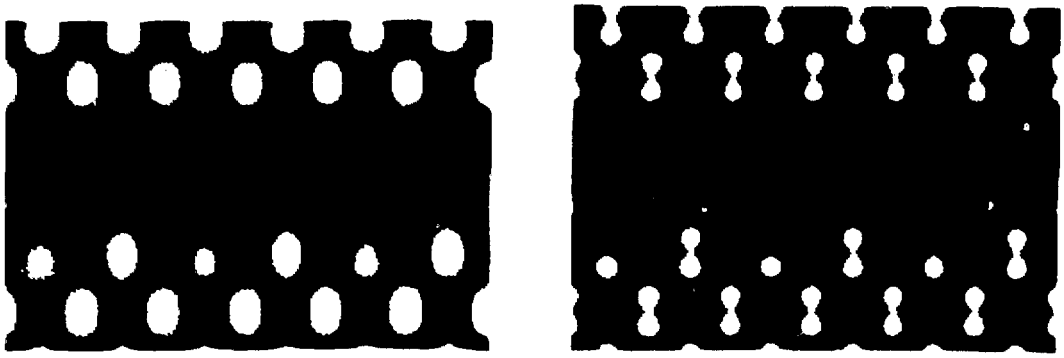

Fig. 19. Simulated images of interfacial ordering in a Si_4Ge_8 superlattice at (a) 100 kV and (b) 300 kV accelerating voltages.

Significant enhancement of the resolution is also anticipated through maximum entropy image restoration techniques. The most likely positions and strengths of the fewest scattering centers needed to account for the distribution of intensity in the image are determined for a given point spread function.[46] Figure 20 shows a reconstruction from a rather poor image of Si⟨110⟩, demonstrating how the fact that the image comes from dumbbells can be extracted from the image with no prior knowledge. The program has rotated the dumbbells somewhat, most probably as a result of some sample tilt, but still gives an average separation of 1.33 Å ± 0.20 for the two columns of a dumbbell, remarkably close to the true value of 1.36 Å. With improved detector efficiencies, it seems reasonable to expect such positional accuracies to

be achievable from individual columns. In addition, the analysis quantifies the relative strengths of the scattering centers which contain the compositional information.

Fig. 20. (a) Z-contrast image of Si(110) and (b) maximum entropy reconstruction indicating the presence of dumbbells.

It is also likely that Z-contrast imaging will be combined with the more traditional methods of compositional mapping. The image provides a means for accurately locating a probe over an individual atomic column from which x-ray or energy loss data could be collected. The high efficiency and sensitivity of modern parallel detection energy loss spectrometers make this technique particularly attractive, and it should soon be possible to combine column-by-column imaging with column-by-column spectroscopy, representing the final merging of high-resolution imaging and analysis on one microscope.

7. Acknowledgements

The authors are grateful to their colleagues at ORNL for collaboration, M. F. Chisholm, R. Feenstra, D. P. Norton, and D. H. Lowndes, also to J.-M. Baribeau and D. C. Houghton for provision of samples, to T. C. Ferridge for the maximum entropy reconstruction which was performed with the Cambridge MemSys 5 software of J. Skilling and S. F. Gull, and to T. C. Estes, J. T. Luck, and S. L. Carney for technical assistance. This research was sponsored by the Division of Materials Sciences, U. S. Department of Energy, under contract DE-AC05-84OR21400 with Martin Marietta Energy Systems, Inc.

8. References

1. L. M. Brown, *J. Phys. F* **11** (1981) 1.
2. S. J. Pennycook, *Contemporary Physics* **23** (1982) 371.
3. C. Colliex and C. Mory, in *Quantitative Electron Microscopy*, eds. J. N. Chapman and A. J. Craven (Scottish Universities Summer School in Physics, Edinburgh, Scotland, 1984) p. 149.

4. G. Ade, *Optic* **49** (1977) 113.
5. J. M. Cowley, *Ultramicroscopy* **2** (1976) 3.
6. A. V. Crewe and J. Wall, *J. Molec. Biol.* **48** (1970) 375.
7. J. Wall, J. Langmore, M. Isaacson, and A. V. Crewe, *Proc. Nat. Acad. Sci. USA* **71** (1974) 1.
8. A. V. Crewe, J. P. Langmore, and M. S. Isaacson, in *Physical Aspects of Electron Microscopy and Microbeam Analysis*, eds. B. M. Siegel and D. R. Beaman (Wiley and Sons, New York, 1975), p. 47.
9. M. S. Isaacson, M. Ohtsuki, and M. Utlaut, in *Introduction to Analytical Electron Microscopy*, eds. J. J. Hren, J. I. Goldstein, and D. C. Joy (Plenum Press, New York, 1979), p. 343.
10. A. Howie, *J. Microsc.* **117** (1979) 11.
11. M. M. J. Treacy and S. B. Rice, *J. Microsc.* **156** (1989) 211.
12. S. J. Pennycook and D. E. Jesson, *Phys. Rev. Lett.* **64** (1990) 938.
13. S. J. Pennycook and D. E. Jesson, *Ultramicroscopy* **37** (1991) 14.
14. D. E. Jesson, S. J. Pennycook, and M. F. Chisholm, *Atomic Scale Structure of Interfaces*, eds. R. D. Bringans, R. M. Feenstra, and J. M. Gibson (Materials Research Society, Pittsburgh, 1990) p. 439.
15. D. E. Jesson and S. J. Pennycook, submitted to *Proc. Roy. Soc.*
16. A. Engel, J. W. Wiggins, and D. C. Woodruff, *J. Appl. Phys.* **45** (1974) 2739.
17. J. M. Gibson and A. Howie, *Chemica Scripta* **14** (1978–79) 109.
18. J. Fertig and H. Rose, *Ultramicroscopy* **2** (1977) 269.
19. C. R. Hall, *Philos. Mag.* **12** (1965) 815.
20. C. R. Hall and P. B. Hirsch, *Proc. Roy. Soc.* **A286** (1965) 158.
21. D. Cherns, A. Howie, and M. H. Jacobs, *Z. Naturforsch.* **28a** (1973) 565.
22. S. J. Pennycook and A. Howie, *Philos. Mag.* **41** (1980) 809.
23. Z. L. Wang and J. M. Cowley, *Ultramicroscopy* **32** (1990) 275.
24. Z. L. Wang and J. M. Cowley, *Ultramicroscopy* **31** (1989) 437.
25. S. Takagi, *J. Phys. Soc. Japn* **13** (1958) 278.
26. Z. L. Wang and J. Bentley, *Ultramicroscopy* **37** (1991) 39.
27. P. A. Doyle and P. S. Turner, *Acta Cryst.* **A43** (1968) 390.
28. S. J. Pennycook, S. D. Berger, and R. J. Culbertson, *J. Microsc.* **144** (1986) 229.
29. H. Fleischmann, *Z. Naturforsch* **15a** (1960) 1090.
30. F. Salvat, *Phys. Rev. A* **43** (1991) 578.
31. D. M. Bird and A. G. Wright, *Acta Cryst* **A45** (1989) 104.
32. K. Kambe, G. Lehmpfuhl, and F. Fujimoto, *Z. Naturforsch.* **29a** (1974) 1034.
33. B. F. Buxton, J. E. Loveluck, and J. W. Steeds, *Philos. Mag.* **A38** (1978) 259.
34. J. Fertig and H. Rose, *Optik* **59** (1981) 407.
35. R. F. Loane, E. J. Kirkland, and J. Silcox, *Acta Cryst.* **A44** (1988) 912.
36. D. E. Jesson and S. J. Pennycook, in *Proc. of the XIIth International Congress for Electron Microscopy*, Vol. 1, eds. L. D. Peachey and D. B. Williams (San Francisco Press, San Francisco, California, 1990) p. 74.
37. S. J. Pennycook and D. E. Jesson, *Acta Metall. Mater.* (1992) in press.

38. M. Kelly and D. M. Bird, *Proc. 49th EMSA* meeting, ed. G. W Bailey and E. L. Hall (San Francisco Press, San Francisco, California, 1991) p. 666.
39. K. Kambe, *Ultramicroscopy* **10** (1982) 223.
40. D. H. Shin, E. J. Kirkland, and J. Silcox, *Appl. Phys. Lett.* **55** (1989) 2456.
41. P. Xu, E. J. Kirkland, J. Silcox, and R. Keyse, *Ultramicroscopy* **32** (1990) 93.
42. O. Scherzer, *J. Appl. Phys.* **20** (1949) 20.
43. A. V. Crewe and D. B. Salzman, *Ultramicroscopy* **9** (1982) 373.
44. J. M. Cowley, in *High Resolution Transmission Electron Microscopy*, eds. P. R. Buseck, J. M. Cowley, and L. Eyring (Oxford University Press, New York, 1988) p. 3.
45. M. Born and E. Wolf, in *Principles of Optics*, 6th Ed. (Pergamon Press, 1980) pp. 333 and 415.
46. S. F. Gull and J. Skilling, *IEE Proc.* **131F** (1984) 646.
47. S. J. Pennycook, in *Annual Review of Materials Science* (1992) in press.
48. D. E. Jesson, S. J. Pennycook, and J.-M. Baribeau, *Phys. Rev. Lett.* **66** (1991) 750.
49. S. J. Pennycook, M. F. Chisholm, D. E. Jesson, D. P. Norton, D. H. Lowndes, R. Feenstra, H. R. Kerchner, and J. O. Thomson, *Phys. Rev. Lett.* **67** (1991) 765.